Chinese Chemical Letters 36 (2025) 110394

Contents lists available at ScienceDirect

Chinese Chemical Letters

journal homepage: www.elsevier.com/locate/cclet

Preparing sub-monolayer metals with continuous coverage spread for high-throughput growth of metal-organic frameworks

Jiayi Lu, Yizhang Li, Hao Jiang, Zhiwen Zhu, Fengru Zheng, Qiang Sun*

Materials Genome Institute, Shanghai Engineering Research Center for Integrated Circuits and Advanced Display Materials, Shanghai University, Shanghai 200444, China

ARTICLE INFO

Article history:
Received 22 June 2024
Revised 27 August 2024
Accepted 30 August 2024
Available online 31 August 2024

Keywords:
Surface-confined metal-organic frameworks
High-throughput preparation
Scanning tunneling microscopy (STM)
Surface science
Stoichiometric design

ABSTRACT

Surface-confined metal-organic frameworks have emerged as versatile structures with a broad spectrum of applications such as nanoelectronics, catalysis, sensing, and molecular storage, owing to their unique structural and electronic properties. However, the exploration and optimization of molecular networks typically involve resource-intensive trial-and-error experiments. The complexity comes from factors like metal nodes, organic ligands, substrates, and the preparation conditions. To address this challenge, high-throughput methodologies have been used in materials exploration. In this work, we explored a high-throughput method for preparing sub-monolayer metals with continuous coverage spread on metal surfaces. By employing a physical mask during metal deposition under ultra-high vacuum conditions, we achieved sample libraries with copper (Cu) and silver (Ag) adatoms on the metal substrates, and constructed surface-supported metal-organic frameworks with varying metal-to-molecule stoichiometric ratios. This approach facilitates the exploration of surface-confined metal-organic frameworks, particularly in terms of varying metal-to-ligand stoichiometric ratios, offering an efficient pathway to unlock the potential of these intricate two-dimensional networks.

Surface-confined metal-organic frameworks are single-layer structures that emerge from the self-assembly of metal atoms and organic ligands supported on solid substrates [1-4]. These two-dimensional structures have stirred immense interest owing to their potential across various applications, such as nanoelectronics [5,6], catalysis [7-9], sensing [10], and molecular storage [11], driven by their unique structural and electronic properties [12,13].

Their properties and functionalities are multifaceted and depend on a multitude of factors [14,15]. This complexity arises from the intricate interplay of variables such as the choice of metal nodes and organic ligands, the nature of the substrate, and the conditions under which self-assembly occurs [16-19]. These variables collectively determine the structural configuration, stability, and performance of molecular networks, thereby influencing their suitability for various applications [20,21]. Owing to the inherent complexity, the designs of molecular structures often necessitate a series of trial-and-error experiments with precise control of the optimal stoichiometry and deposition rates of the metal and organic components, which can be particularly challenging and resource-intensive. Consequently, there is a growing impetus for developing more efficient strategies to expedite the screening and optimization of molecular nanostructures with varied compositions and structures.

Over recent decades, the advancement of high-throughput methodologies has profoundly revolutionized materials exploration across various domains [22]. This revolution is not limited to, but notably includes, the rapid synthesis of high-temperature superconductors (high-Tc) [23,24], the large-scale fabrication of monolayer transition metal dichalcogenides [25], and the development of novel porous materials [26]. These developments represent significant advances, underscoring the pivotal role of high-throughput techniques in enabling rapid, efficient, and scalable exploration and synthesis of materials [27]. We have recently developed a high-throughput method in the preparation of spatially addressable libraries of supramolecular self-assemblies on surfaces [28]. This is achieved by creating samples of continuous spreads of molecular coverage through physical masking techniques beyond the standard molecular deposition processes. However, in high-throughput growth techniques for surface-supported metal-organic frameworks, the systematic exploration of varying the concentration of another crucial component, namely, the metal nodes, remains unexplored. This oversight represents a gap in our understanding and structure exploration, as the concentration of metal

* Corresponding author.
E-mail address: qiangsun@shu.edu.cn (Q. Sun).

https://doi.org/10.1016/j.cclet.2024.110394
1001-8417/

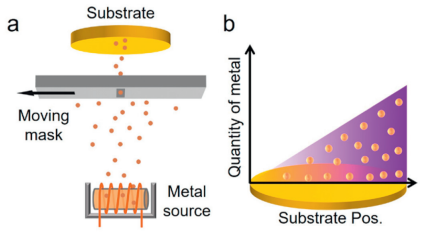

Fig. 1. The sample preparation. (a) Schematic illustration of the metal deposition process employing a physical mask. Metal atoms (represented by orange dots) sublime from a metal source and only those atoms traverse the slit of the mask can accumulate on a substrate. The substrate-mask relative motion and time intervals of the moving mask are controlled to modulate the metal atom distribution on the substrate. (b) Correlation between the substrate position (Substrate Pos.) and the quantity of the deposit metals. The shaded gradient indicates the progressive increase in metal atom density across the substrate.

nodes is critically influencing the structural and functional properties.

In this work, we report the preparation of sub-monolayer metals with continuous coverage spread on metal surfaces. This is achieved by a high-throughput preparation method (schematically illustrated in Fig. 1) by introducing a physical mask into the typical preparation chamber under ultra-high vacuum (UHV). By controlling the relative movement between the substrate and the mask with a slit between the metal evaporator and substrate during source sublimation, we obtained sample libraries with copper (Cu) and silver (Ag) adatoms of continuous coverage spread across the substrate, respectively. The resultant sample libraries allow for the exploration of surface-confined metal-organic frameworks, particularly in terms of varying metal-to-ligand stoichiometric ratios. Our approach provides an efficient pathway to unlock the potential of these intricate two-dimensional networks.

Given the constraints of limited substrate sizes (typically within a few millimeters), achieving a delicate control of the beams of metal atoms during evaporation is essential for efficient parallel synthesis for our methodology. To address this issue, we have implemented a physical mask with a narrow slit, strategically positioned between the substrate and the metal evaporators as indicated in Fig. 1a. This configuration ensures that during the deposition phase, only those which successfully traverse the slit are deposited onto the specific regions of the substrate. This technique not only enhances precision in the placement of deposited species but also improves the uniformity and specificity of the deposition process.

We employed scanning tunneling microscopy (STM) to observe and verify both the spatial distribution of the deposited metal atoms and the self-assembled behaviours of the molecular precursors. These observations were conducted under liquid-nitrogen temperature conditions (~77.8 K) and in an ultra-high vacuum (UHV) environment to prevent contamination and maintain the integrity of the samples. The molecularly resolved STM imaging is instrumental in understanding the subtle intricacies involved in the formation of sub-monolayer metals and the self-assembly of molecular precursors. More details of experiments can be found in note S4 (Supporting information).

We first focused on the deposition of Cu atoms onto the Au (111) substrate, with the objective of achieving a controlled gradient distribution. As displayed in Fig. 2, the deposition process resulted in a gradient of Cu atom coverage across the substrate as assessed using STM imaging at a series of regions. Fig. 2b indicates the statistical analysis of the copper quantities at different macroscopic positions along the horizontal axis of the substrate.

In the intended Cu-free regions (Pos. 1), a typical clean Au (111) surface is evident with only the characteristic herringbone reconstruction (Fig. 2e). This is consistent with the expected morphology of a clean Au (111) surface under UHV conditions, which typically exhibits herringbone patterns due to the surface stress caused by the lattice deformation between the Au layers [29]. At the regions around Pos. 2, we observed the initial stage of Cu decorations, where the Cu atoms preferentially nucleate at Au step edges before evolving into larger, more densely packed islands. In regions of greater Cu atom coverage (Pos. 3-5 shown in Fig. 2e), the metal atoms tend to grow both along the step edges and on the terraces. This directed growth ultimately leads to the formation of reconstructed Cu islands. In these islands, the Cu atoms present a morphology reminiscent of the underlying Au (111) surface, yet they display a more pronounced level of disorder (Fig. S2c in Supporting information) [30]. The height of the Cu islands relative to the supporting Au terrace is approximately 170 pm as demonstrated in Figs. 2c and d. The apparent height is slightly lower than that of the Au (111) and Cu (111) monatomic steps, suggesting a partial embedding of Cu atoms into the Au surface layer [31]. Such embedding implies a degree of Cu incorporation or interdiffusion at the interface, which may account for the observed disorder in the corrugation patterns of the Cu islands [30]. The transition from Cu-depleted to Cu-rich regions is revealed by the statistical analysis of the Cu coverage, highlighting the high level of precision achieved with this deposition process.

The successful fabrication of the Cu gradient samples allows further exploration of the dependence of varying metal-ligand stoichiometric ratios on the surface-supported metal-organic nanostructures. Au atoms tend to coordinate with pyridyl groups, forming motifs similar to those created by Cu coordination (note S2 in Supporting information). In contrast, on Ag (111), pyridyl functionalized molecules do not coordinate with Ag adatoms, ensuring that all the observed two-fold coordinating nanostructures are formed with the deposited Cu atoms. We then prepared an Ag (111) substrate with gradient distributions of Cu atoms, followed by the deposition of 1,3,5-tris[4-(pyridin-4-yl)phenyl]benzene (ext-TPyB) molecules and ~423 K annealing as illustrated in Fig. 3. Such preparation yields samples with varying metal-ligand stoichiometric ratios on the substrate. We utilized high-resolution STM imaging to assess distinct macroscopic areas along the horizontal directions as schematically shown in Fig. 3a.

Fig. 3c displays typical STM images of four distinct areas, revealing a clear progression from close-packed molecular structures (identified as phase I) to porous molecular networks (phase II). Such a gradient molecular coverage on the substrate is more evident from the statistically analyzed histogram shown in Fig. 3b. Phase I, formed in Cu-free regions, comprises solely ext-TPyB molecules, which are stabilized through intermolecular hydrogen bonding since the Ag atoms on the Ag (111) substrate do not participate in the coordination with pyridyl ligands [32]. Whereas in Cu-rich regions (Pos. 4), we find that the dominant phase is phase II, where the 2-fold coordination with Cu adatoms emerges as the prevalent driving force guiding the molecular assembly, leading to the formation of porous honeycomb networks.

At Pos. 2 and 3, the original hydrogen bonding nanostructures (Phase I) are perturbed by the introduction of Cu coordination (Phase II) [32,33]. The distinct contrast between the two phases, evident in the large-scale STM images, underscores the delicate interplay between the hydrogen bonding interaction and metal coordination. The balance can be finely modulated by controlling the local Cu adatom concentration. The proportion of Phase II increases in correlation with the coverage of Cu atoms as clearly indicated by the statistical analysis in Fig. 3b. Notably, the overall amount of Cu

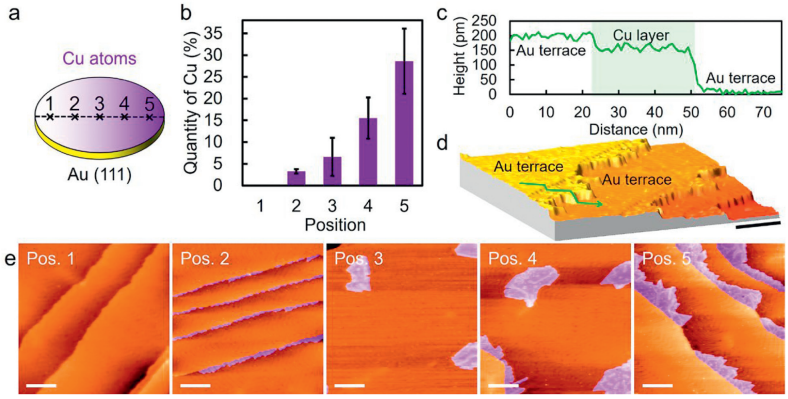

Fig. 2. Gradient distribution of Cu atoms on Au (111). (a) Schematic of the Au (111) substrate with numbers indicating different macroscopic locations. The darkness of the purple color suggests the coverage of the deposited Cu atoms. (b) The quantity percentage of Cu atoms across different positions on the Au (111) substrate, calculated from the coverage of Cu atomic islands, illustrating an increase in coverage from position (Pos.) 1 to 5. (c) Line-scan profile from the green arrow in (d) showing two Au terraces and the monolayer Cu island adsorbing on the lower Au terrace. (d) 3D topographic image of the Cu layers deposited on the Au (111) substrate. Scale bar: 40 nm. Scanning parameters: $I_t = 60$ pA, $V_b = -2.5$ V. (e) Series of large-scale STM images from Pos. 1 to 5 on Au (111), displaying the increased coverage of Cu atoms (marked with purple shading). Scale bars: 40 nm. Scanning parameters are $I_t = 60$ pA, $V_b = -2.5$ V for Pos. 1 and Pos. 3-5; $I_t = 60$ pA, $V_b = -2.0$ V for Pos. 2.

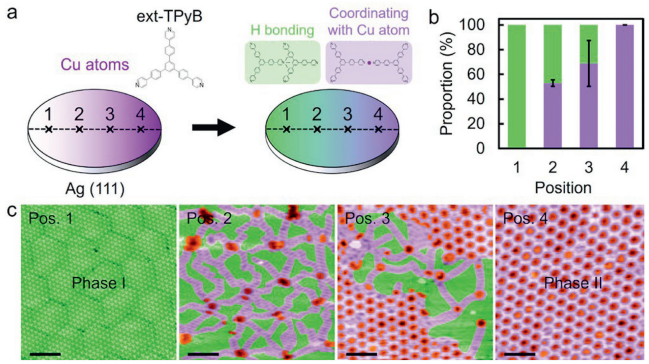

Fig. 3. Self-assembled nanostructures with gradient distribution of metals. (a) Chemical structure of the ext-TPyB molecule and schematics of the Ag (111) surface with indexed positions after the deposition of ext-TPyB. In Cu-deficient areas (left), the nanostructures are primarily driven by intermolecular hydrogen bonding (Phase I marked by green shading), whereas in Cu-rich regions, the metal-organic nanostructures prevail (Phase II marked by purple shading). (b) Histograms indicating the proportions of Phase I (green) and Phase II (purple) across different substrate positions indicated in (a). (c) Typical large-scale topographic images at Pos. 1-4, revealing the evolution in self-assemblies of ext-TPyB on the surface. Scale bars: 10 nm. Scanning parameters are $I_t = 160$ pA, $V_b = -1.3$ V for Pos. 1; $I_t = 100$ pA, $V_b = -2.0$ V for Pos. 2 and Pos. 3; $I_t = 70$ pA, $V_b = -2.0$ V for Pos. 4.

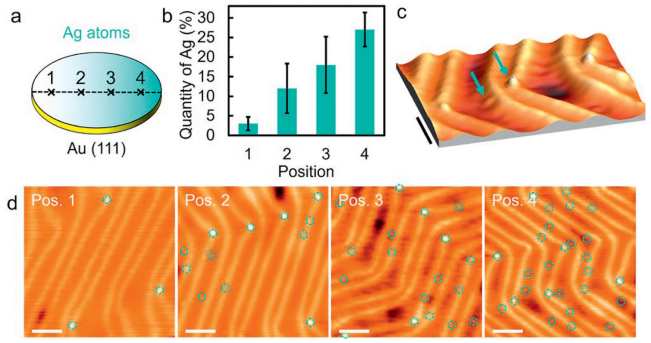

Fig. 4. Gradient distribution of Ag atoms on Au (111). (a) Schematic of the Au (111) substrate with numbers suggesting different macroscopic locations. The darkness of the cyan color suggests the coverage of Ag. (b) The quantity percentage of Ag at different positions on the Au (111) substrate, calculated from the number of Ag adsorbates visible in the STM images, with 100 adsorbates per 900 nm^2 as the reference of 100%. (c) 3D topographic view of the Ag atoms on the Au (111) substrate. The arrows indicate the adsorbing Ag atoms. Scale bar: 5 nm. Scanning parameters: $I_t = 100$ pA, $V_b = -1.5$ V. Ag atoms are indicated by cyan arrows. (d) Typical STM images at Pos. 1-4, showing the varying coverage of Ag (highlighted with cyan dashed circles). Scale bars: 6 nm. Scanning parameters are $I_t = 100$ pA, $V_b = -1.5$ V for Pos. 1-4.

is lower than that shown in Fig. 2 to avoid an excessive surplus of Cu.

To further demonstrate the generality of this high-throughput method, we have attempted to grow gradient coverage of Ag atoms on the Au substrate (Fig. 4). Single-crystal Au and Ag both exhibit a face-centered cubic (FCC) lattice structure. The similarity in lattice parameters between Au and Ag (~4.08 Å) facilitates the formation of a solid solution in the solid state. Therefore, Au and Ag atoms can interchangeably occupy positions in their lattices, resulting in minimal lattice distortion [34]. After depositing Ag on the Au (111) surface, we can identify two kinds of Ag adsorbates as reflected in the 3D topographic image in Fig. 4c. One is located at the elbow site of the herringbone reconstruction with an apparent height of ~16.8 pm, and the other resides in-between or on the herringbone ridges with the apparent height at the same level of the top layer of the surface [35,36]. This is in contrast to the Cu adsorbates which nucleate to island structures.

We are able to deduce the quantity of Ag at different macroscopic positions by counting the Ag adsorbates from the high-resolution STM imaging capturing the characteristic features of Ag atoms on Au (111) (Fig. 4d). The quantity of Ag is statistically analyzed (Fig. 4b), unfolding the expected gradient distribution. These results further support our technique's potential for designing and screening molecular nanostructures of specific properties. Consequently, the influence of Ag coverage on the self-assembled molecular nanostructures is studied and the results can be found in note S3 (Supporting information).

Finally, we attempt to create a gradient distribution of Cobalt (Co) atoms on Au (111). Co is distinct from the Ag and Cu with a much higher melting point and, correspondingly, a considerably lower vapor pressure at equivalent temperatures. Consequently, to evaporate Co atoms into the vacuum chamber, higher temperatures or energies are necessary. This requirement of elevated temperature means that the Co atoms, once evaporated, possess higher kinetic energies compared to their Cu and Ag counterparts.

Our experiments indeed reflect a different scenario from the cases of Cu and Ag. We applied the same deposition process with the aim of producing compositionally varying samples on Au (111).

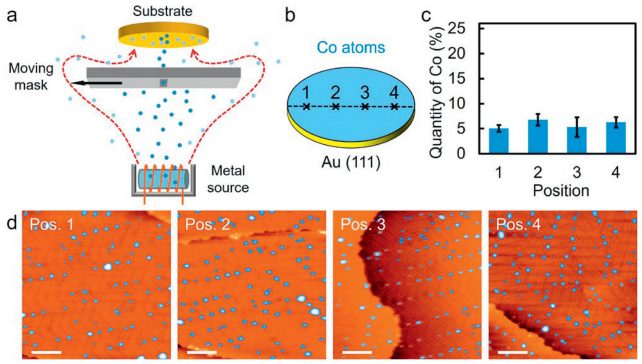

Fig. 5. Attempt to produce gradient distribution of Co atoms. (a) Schematic representation of the metal deposition process. For metals requiring high sublimation temperatures, blue dots symbolize sublimed metal atoms, and red dashed arrows indicate possible alternative pathway for atom deposition on the substrate. (b) Schematic of the metal substrate with numbers indicating the macroscopic positions. (c) The quantity percentage of Co atoms across different macroscopic positions on the Au (111) substrate, calculated from the coverage of Co islands, clearly indicating a relatively uniform distribution. (d) Typical large-scale STM images at Pos. 1-4. The Co clusters on the substrate are marked by the blue shading. Scale bars: 20 nm. Scanning parameters are $I_t = 40$ pA, $V_b = -1.5$ V for Pos. 1, Pos. 3, and Pos. 4; $I_t = 50$ pA, $V_b = -1.5$ V for Pos. 2.

As depicted in the coverage analysis and STM images in Fig. 5, there is no sign of gradient distribution of the Co adsorbates, and we only obtained a uniform distribution of the Co clusters on the substrate. The STM images in Fig. 5d reveal the formation of Co clusters preferably at the elbow sites of the herringbone reconstruction across the substrate [37]. Despite the implementation of the masking technique, the high sublimation temperature of Co is attributed to suppress the intended high-throughput growth of the Co-adsorbing samples [38]. We hypothesize that during the metal evaporation process, the high kinetic energies of the evaporated atoms make them follow an alternative pathway to reach the substrate, as depicted by the red arrows in Fig. 5a. This occurs irrespective of the obstruction posed by the mask.

In summary, we have successfully demonstrated a high-throughput method for preparing sub-monolayer metals with continuous coverage on surfaces. This was achieved using a physical masking technique for the deposition of metal adatoms on substrates under UHV conditions. Our approach has facilitated the creation of gradient distributions in the coverage of Cu and Ag atoms across metal substrates. This method offers a valuable and versatile opportunity for the rapid discovery and screening of metal-organic nanostructures. We also address the limitations of the moving mask technique in our study, specifically when attempting to grow a gradient coverage of Co, a metal with a high evaporation temperature, on the Au substrate. The findings presented in this report may pave the way for a systematic exploration of surface nanostructure at varying metal-to-ligand sociometrical ratios and the advancement of two-dimensional materials composed of multiple components.

Declaration of competing interest

The authors declare the following financial interests/personal relationships which may be considered as potential competing interests:

Qiang Sun reports financial support was provided by Shanghai University.

CRediT authorship contribution statement

Jiayi Lu: Writing – review & editing, Writing – original draft, Formal analysis, Data curation. **Yizhang Li:** Writing – review & editing, Data curation. **Hao Jiang:** Writing – review & editing, Data curation. **Zhiwen Zhu:** Writing – review & editing, Data curation. **Fengru Zheng:** Writing – review & editing, Methodology, Data curation. **Qiang Sun:** Writing – review & editing, Supervision, Funding acquisition, Conceptualization.

Acknowledgment

This work was supported by National Natural Science Foundation of China (Nos. 22072086, 22302120).

Supplementary materials

Supplementary material associated with this article can be found, in the online version, at doi:10.1016/j.cclet.2024.110394.

References

[1] R. Kaminker, L. Motiei, A. Gulino, et al., J. Am. Chem. Soc. 132 (2010) 14554–14561.
[2] S. Stepanow, N. Lin, J.V. Barth, K. Kern, J. Phys. Chem. B 110 (2006) 23472–23477.
[3] J. Lu, D. Nieckarz, H. Jiang, et al., ACS Nano 17 (2023) 20194–20202.
[4] Z. Zhu, J. Lu, F. Zheng, et al., Angew. Chem. Int. Ed. 61 (2022) e202213503.
[5] S. Wu, Z. Li, M. Li, et al., Nat. Nanotechnol. 15 (2020) 934–940.
[6] M. Mabrouk, R. Hayn, H. Denawi, R. Ben Chaabane, J. Magn. Magn. Mater. 453 (2018) 48–52.
[7] A. Dhakshinamoorthy, A.M. Asiri, H. Garcia, Adv. Mater. 31 (2019) 1900617.
[8] R. Wei, P. You, H. Duan, et al., J. Am. Chem. Soc. 144 (2022) 17487–17495.
[9] L. Ma, J.M. Falkowski, C. Abney, W. Lin, Nat. Chem. 2 (2010) 838–846.
[10] L.E. Kreno, K. Leong, O.K. Farha, et al., Chem. Rev. 112 (2012) 1105–1125.
[11] S.O. Parreiras, J.M. Gallego, D. Écija, Chem. Commun. 59 (2023) 8878–8893.
[12] K. Zhou, Y. Zhou, Z. Jia, et al., Cell Rep. Phys. Sci. 4 (2023) 101656.
[13] C. Wang, D. Liu, W. Lin, J. Am. Chem. Soc. 135 (2013) 13222–13234.
[14] J. Liu, T. Lin, Z. Shi, et al., J. Am. Chem. Soc. 133 (2011) 18760–18766.
[15] L. Dong, Z.A. Gao, N. Lin, Prog. Surf. Sci. 91 (2016) 101–135.
[16] H. Li, M. Eddaoudi, M. O'Keeffe, O.M. Yaghi, Nature 402 (1999) 276–279.
[17] D. Zhao, D.J. Timmons, D. Yuan, H. Zhou, Acc. Chem. Res. 44 (2011) 123–133.
[18] Z. Zhu, J. Lu, S. Yuan, et al., J. Phys. Chem. Lett. 15 (2024) 1985–1992.
[19] H. Jiang, Y. He, J. Lu, et al., ACS Nano 18 (2024) 1118–1125.
[20] T.R. Cook, Y.R. Zheng, P.J. Stang, Chem. Rev. 113 (2013) 734–777.
[21] A. Vishina, O.Y. Vekilova, T. Björkman, et al., Phys. Rev. B 101 (2020) 094407.
[22] Y. Liu, Z. Hu, Z. Suo, et al., Sci. China Technol. Sci. 62 (2019) 521–545.
[23] J. Yuan, V. Stanev, C. Gao, et al., Supercond. Sci. Technol. 32 (2019) 123001.
[24] X.D. Xiang, X. Sun, G. Briceño, et al., Science 268 (1995) 1738–1740.
[25] M. Seol, M.H. Lee, H. Kim, et al., Adv. Mater. 32 (2020) 2003542.
[26] I.G. Clayson, D. Hewitt, M. Hutereau, et al., Adv. Mater. 32 (2020) 2002780.
[27] S.K. Suram, J.A. Haber, J. Jin, J.M. Gregoire, ACS Comb. Sci. 17 (2015) 224–233.
[28] J. Lu, H. Jiang, Y. Yan, et al., ACS Nano 16 (2022) 13160–13167.
[29] P. Li, F. Ding, Sci. Adv. 8 (2022) eabq2900.
[30] F. Grillo, H. Früchtl, S.M. Francis, N.V. Richardson, New J. Phys. 13 (2011) 013044.
[31] F. Xiang, C. Li, Z. Wang, et al., Surf. Sci. 633 (2015) 46–52.
[32] F. Zheng, J. Lu, Z. Zhu, et al., ACS Nano 17 (2023) 17545–17553.
[33] A.I. Fadeeva, V.A. Gorbunov, O.S. Solovyeva, et al., J. Phys. Chem. C 124 (2020) 11506–11515.
[34] T. Guo, Y. Tan, Nanoscale 5 (2013) 561–569.
[35] F. Hanke, J. Björk, Phys. Rev. B 87 (2013) 235422.
[36] H. Oka, K. Sueoka, Jpn. J. Appl. Phys. 44 (2005) 5430.
[37] I. Chado, S. Padovani, F. Scheurer, J.P. Bucher, Appl. Surf. Sci. 164 (2000) 42–47.
[38] F.M. Wachi, D.E. Gilmartin, J. Chem. Phys. 57 (1972) 4713–4716.